

Multi-level observation of magneto-acoustic cut-off frequency above sunspots

Ding Yuan¹, R. Sych², V. E. Reznikova³, and V. M. Nakariakov^{1,4}

¹ Centre for Fusion, Space and Astrophysics, Department of Physics, University of Warwick, Coventry CV4 7AL, UK
e-mail: Ding.Yuan@warwick.ac.uk

² Institute of Solar-Terrestrial Physics, Russian Academy of Science, Siberian Branch, 126a Lermontov st., Irkutsk 664033, Russia

³ Center for Mathematical Plasma Astrophysics, Department of Mathematics, KU Leuven, Celestijnenlaan 200B box 2400 BE-3001 Leuven, Belgium

⁴ Central Astronomical Observatory at Pulkovo of the Russian Academy of Sciences, 196140 St Petersburg, Russia

January 16, 2013

ABSTRACT

Context. The cut-off frequency of magneto-acoustic gravity (MAG) waves is known to be lowered by the inclined magnetic field. This effect allows low-frequency waves to penetrate into the upper atmosphere and the corona.

Aims. We estimate the modification of the cut-off frequency at various heights and reconstruct the inclination of the magnetic field according to the magnetoacoustic-gravity wave theory in a stratified solar atmosphere permeated by a uniform magnetic field.

Methods. We used the Pixelised Wavelet Filtering (PWF) method to compute narrow-band power maps of SDO/AIA imaging datasets in the 1700 Å, 1600 Å and 304 Å bandpasses that correspond to different heights. The cut-off frequency was defined as contours where the spectral power dropped to the median level. It was measured as a function of the spatial location. We inferred the magnetic field inclination according to the MAG wave theory in the low- β limit and compared it with the potential field extrapolation.

Results. We analysed intensity oscillations in a symmetric sunspot AR11131 (08 Dec 2010) and an asymmetric sunspot AR11330 (27 Oct 2011). We reconstructed the magnetic field inclination in the radial direction for the symmetric sunspot and in both radial and azimuthal directions for the asymmetric sunspot.

Conclusions. We observed 3D variation of the main oscillation periods in sunspots. We found that shorter-period oscillations were mostly constrained in sunspot umbrae, while longer-period oscillations formed an annular shape enclosing the umbra. Longer periods are found to be distributed further away from the sunspot centre. Our results indicate that 3-min oscillation are generated in the chromosphere, possibly by the acoustic resonator model, while 5-min and longer-period oscillations seemed to originate in a level under the photosphere. The reconstructed field inclinations gives the values of the field inclination that are systematically larger than the values obtained by the potential field extrapolation. The inclined magnetic field line can account for 60-80% of cut-off frequency lowering only.

Key words. Sun: atmosphere - Sun: UV radiation - Sun: oscillations - Sun: sunspots -Sun: magnetic topology

1. Introduction

Mangetoacoustic gravity (MAG) waves in the solar atmosphere are subject to strong dispersion: their properties depend strongly on their frequency. In particular, the parameters of the solar atmosphere determine the MAG cut-off frequency. MAG waves with frequencies below the cut-off value become evanescent, and therefore cannot reach the upper layers of the solar atmosphere. The cut-off value also determines the oscillating frequency of MAG waves as the response of the atmosphere to a broadband (e.g. impulsive) excitation (e.g. Suematsu et al. 1982; Botha et al. 2011). The cut-off frequency for MAG waves was derived for a stratified isothermal solar atmosphere permeated by a uniform magnetic field (Bel & Leroy 1977; Zhugzhda & Dzhililov 1984). It generally depends on the local plasma β ($\beta = 2\mu_0 p/B^2 = 2c_s^2/\gamma V_A^2$, where p is the gas pressure, μ_0 is the magnetic permeability in vacuum space, B is the magnetic field strength, V_A is the local Alfvén speed, c_s is the local sound speed, and $\gamma = 5/3$ is the adiabatic index) and the magnetic field inclination ϕ . In the high- β regions ($\beta \gg 1$, e.g. the photosphere and chromosphere of the quiet Sun), it is reduced into the pure acoustic cut-off frequency

$\nu_0 = \gamma g/4\pi c_s = 5.2$ mHz (with the corresponding cut-off period $p_0 = 3.2$ min), where $g = 274$ m/s is the gravitational acceleration, and $c_s = 7$ km/s is the sound speed estimated for typical chromospheric conditions. In the low- β approximation ($\beta \ll 1$, e.g. in a sunspot or coronal active region), the cut-off frequency is modified by the magnetic inclination $\nu_{ac} = \nu_0 \cos \phi$ (Bel & Leroy 1977)¹. This helps explaining the existence of low-frequency waves in the corona, which are believed to carry a larger portion of energy flux than its high-frequency counterpart (e.g. Fontenla et al. 1993; Jefferies et al. 2006). Also, the study of the effect of the cut-off frequency on compressive waves observed in the solar atmosphere provides us with a seismological tool for the determination of the local geometry of the magnetic field.

According to Bel & Leroy (1977), the low-frequency (long-period) waves are able to penetrate the upper solar atmosphere, along the magnetic concentrations, e.g. sunspots, pores, which

¹ The derivations in Bel & Leroy (1977) contain obvious misprints, a follow-up theoretical study will redo the derivation. However the numerical results and figures are reliable. In this work, we use the trustworthy extreme case of $\beta \ll 1$

work as MAG waveguides. It was suggested that, due to the effect of the magnetic inclination, the 5-min oscillations appear in the chromospheric spicules (De Pontieu et al. 2004) and in coronal loops at active regions (De Moortel et al. 2002; De Pontieu et al. 2005). de Wijn et al. (2009) observed the propagation of solar global p -modes to the chromosphere through the inclined magnetic fields at the periphery of plage regions. Other observations of long-period oscillations in the corona could be attributed to channelling by the inclined field as well (see e.g. Wang et al. 2009; Marsh et al. 2009; Yuan et al. 2011).

A direct observation of the magnetoacoustic cut-off in a sunspot has been performed with full Stokes (I, U, V, Q) spectropolarimetry (see Fig. 5 in Bloomfield et al. 2007). The authors found that the cut-off frequency closely followed the magnetic field modification in the strong-field limit ($\beta \ll 1$) of Bel & Leroy (1977). However no further examination was done to compare the information with the magnetic inclination inverted by full Stokes observables. It appeared that the correlation and phase difference of the time series of the intensity variation obtained at various heights of the solar atmosphere looked more realistic when the offsets at the spatial location were corrected by considering the magnetic inclination (Bloomfield et al. 2007). McIntosh & Jefferies (2006) studied the travel time of narrow-band signals around a sunspot and found good consistency with the prediction of Bel & Leroy (1977) for both the quiet sun ($\beta \gg 1$) and a sunspot ($\beta \lesssim 1$). Tziotziou et al. (2006) applied the empirical formula $\nu_{\text{peak}}(\phi) \approx 1.25\nu_{\text{ac}}(\phi)$, where ν_{peak} denotes the peak frequency at each location, ν_{ac} indicates the corresponding magnetoacoustic cut-off frequency, to the waves observed in a sunspot's chromosphere, and estimated the magnetic field inclination $\phi = \arccos[\nu_{\text{peak}}/(1.25 \times \nu_0)]$ (Bogdan & Judge 2006). Reznikova et al. (2012) compared the spectra and phase relations of the UV and EUV emission intensity at various heights of the solar atmosphere to identify the features of upwardly propagating waves and found that the variation of the cut-off frequency across the umbra was consistent with Bel & Leroy (1977). The follow-up study (Reznikova & Shibasaki 2012) compared the observational MAG cut-off frequencies in AIA 304 Å with the values obtained by the potential field extrapolation (Sakurai 1982) and found good agreement.

In Bel & Leroy (1977), an adiabatic plasma was implicitly assumed, while in the photosphere and chromosphere, radiative loss is of significance. Centeno et al. (2006, 2009) used a linear wave equation with a radiative cooling term and explained well the observed phase delay and wave amplitude variation with height in both sunspots and pores. A detailed study using multiple spectral lines formed at different heights was presented in Felipe et al. (2010). The connectivity of different layers of the atmosphere determined by the phase difference and power amplification was demonstrated. Therefore, the study of the cut-off frequency can also retrieve the plasma parameters associated with radiative loss.

The cut-off frequency detected in a sunspot atmosphere is a good indicator of local plasma parameters, therefore it can be used to diagnose the local atmosphere, e.g. temperature, magnetic inclination. In our study, we present the observation of the spatial distribution and height variation of the cut-off frequency with SDO/AIA (Lemen et al. 2011; Boerner et al. 2011) and inferred the magnetic field inclination. The observational results were used for the reconstruction of the 3D geometry of the magnetic field. The information was deployed to diagnose the magnetic field inclination. In this paper, we present the analysed data sets in Sec. 2. The methods are summarised in Sec. 3. Then we

compare the diagnostic results with the potential field extrapolation in Sec. 4, and conclusions are given in Sec. 5.

2. Observations

We selected two large sunspots associated with well-developed active regions in the corona, where outwardly propagating EUV disturbances were persistently detectable. We chose good observation intervals without disruptions from either flares or other transient events. The observation intervals correspond to the days when the sunspots were crossing the central meridian: they were least affected by Wilson depression (Loughhead & Bray 1958) and were well exposed for imaging.

The first sunspot was associated with AR11131 situated near the 30° latitude in the northern hemisphere. It crossed the central meridian on 08 Dec 2010. It consisted of a strong magnetic concentration of the south polarity, while the north polarities were spread sparsely to the west and north of the central sunspot, therefore the sunspot had a pretty symmetric shape without any trailing sunspot, see Fig. 1 (top). We used AIA data sets of 1600 Å, 1700 Å and 304 Å from 02:30 to 03:30 UT on 08 Dec 2010. The cadence time was 24 s for 1600 Å and 1700 Å images, and 12 s for 304 Å images. This sunspot was also analysed in Reznikova et al. (2012); Reznikova & Shibasaki (2012).

The second sunspot chosen for this study was the leading main sunspot on the eastern part of active region AR11330 situated slightly to the north of the solar equator. The trailing sunspot group of north polarity was about 150 Mm to the main sunspot. It formed into a non-symmetric shape with a protrusion due to the tearing of the other polarity (see B_{LOS} in Fig. 1 (e)). The shape was inherited at the temperature minimum (1700 Å, see Fig. 1 (f)), the photosphere and transition region (1600 Å, see Fig. 1 (g)). In the chromosphere (304 Å, Fig. 1 (h)), the shape was less pronounced and was replaced by a far-extending fan structure. The study of propagating EUV disturbances in the coronal fan over this sunspot was presented in Yuan & Nakariakov (2012). We used one-hour data sets from 04:00 to 05:00 UT on 27 Oct 2011 in 1700 Å, 1600 Å and 304 Å. The instrumentation and data preparation are presented in Yuan & Nakariakov (2012). The cadence time was 24 s and 12 s for EU and EUV images, respectively.

3. Methods

3.1. Power map by Pixelised Wavelet Filtering

The Pixelised Wavelet Filtering (PWF) method was developed by Sych & Nakariakov (2008). It is based on the wavelet transform and is well validated in determining the spatial, temporal and phase structure of oscillations in an imaging cube $I_\lambda(x, y, t)$, where λ is the wavelength of the data channel, x , y and t are the discrete spatial locations and the measuring times, respectively. It gives the spatial distribution of the amplitude (power), frequency and phase of a signal in the spectral interval of interest.

For data sets $I_\lambda(x, y, t)$, we performed PWF analysis and obtained narrow-band power maps $P_\nu^\lambda(x, y)$ (or $P_p^\lambda(x, y)$, where $p = \nu^{-1} = 2, \dots, 20$ min with the resolution of $dp = 0.1$ min). In a sunspot, the power distribution normally forms a filled disk (short periods / high frequencies) or a power ring (long period / low frequencies) concentric at the sunspot centre (e.g. Sych & Nakariakov 2008; Reznikova et al. 2012). Therefore, to facilitate quantitative analysis, the power maps were transformed into a polar coordinate system with the origin coinciding with

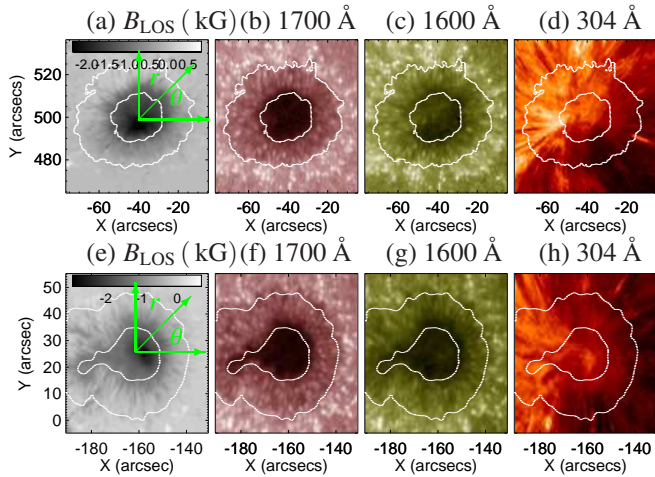


Fig. 1. Multi-instrumental imaging of AR11131 (top, 08 Dec 2010) and AR11330 (bottom, 27 Oct 2011) and the underlying sunspots at different heights. (a) and (e): The LOS magnetic field strength determined with HMI. The polar coordinate systems used in this study are overlaid. (b) - (d) and (f) - (h): AIA intensity images on logarithmic scales at different observational wavelengths show different levels of the sunspots and the associated active regions. In order of increasing heights of the observed levels, the displayed images illustrate the temperature minimum level (1700 Å), upper photosphere and transition region (1600 Å), and the chromosphere (304 Å). The dotted lines show the border of the sunspot umbra and penumbra determined with the 4500 Å image.

1 the sunspot centre $P_v^1(r, \theta)$, where r is the distance to the sunspot
2 centre, θ is the polar angle relative to the horizontal line pointing
3 to the solar west (see Fig. 1 (a) and (e)).

4 For the power maps $P_v(r, \theta)$, the denotation λ is dropped to
5 refer to the general case that is applicable to all wavelengths.
6 We computed the maximum power at each location $P_{\max}(r, \theta)$
7 (see panel (a) in Fig. 4, Fig. 5 and Fig. 6). The correspond-
8 ing peak period is $p_{\text{peak}}(r, \theta)$ (see panel (b) in Fig. 4, Fig. 5 and
9 Fig. 6). The dependence of $p_{\text{peak}}(r, \theta)$ shows the spatial distribu-
10 tion of the period with the dominant oscillating power, while
11 $P_{\max}(r, \theta)$ illustrates the significance of these oscillations. The
12 variance of the spectral power over the spectrum for each pixel
13 was also calculated, $\text{Var}(r, \theta) = \text{Var}(P_v(r, \theta))_v^2$ (see Fig. 4 (d)).
14 This value is a good indicator of the significance of the signal at
15 a specific location. To estimate the 1σ noise level, we took the
16 average over the spectrum $\sigma(r, \theta) = \langle P_v(r, \theta) \rangle_v$ (see example in
17 Fig. 4(e)). For the analysis of the symmetric sunspot, a further
18 averaging over the polar angle θ was performed to reduce the θ
19 dimension. Table 1 summarises the denotations and their physi-
20 cal meanings in both 1D and 2D cases.

21 Several typical narrow-band power maps obtained in 304 Å
22 bandpass on 08 Dec 2010 are shown in Fig. 2 (also see Fig. 7 of
23 Reznikova et al. 2012). For the periods less than 3.2 min (fre-
24 quencies greater than 5.2 mHz), the dominant power fills up the
25 umbra region. The inhomogeneity of the power distribution impli-
26 es a fine structure in the umbra (see the study in Jess et al.
27 2012, using imaging data with a resolution of 50 km/pixel in
28 contrast to 430 km/pixel of AIA images). For the periods greater
29 than 3.2 min, the power of significant oscillations is normally
30 concentrated in an annular structure enclosing the umbra. The
31 annulus expands with the increasing period. We interpret this

² The subscript v means the operation(s) along the spectral dimension. With the same philosophy, the subscripts θ and r mean the operation(s) along the polar angle dimension and radial distance dimension, respectively.

32 phenomenon as modification of the cut-off frequency by the in-
33 clined magnetic field (Bel & Leroy 1977; De Pontieu et al. 2004,
34 2005; McIntosh & Jefferies 2006). This is also confirmed by the
35 phase analysis in Reznikova et al. (2012), they shows upward
36 propagating wave feature in the same sunspot AR11131. The
37 physics does not change significantly in sunspot AR11330, but
38 only the morphology. As the magnetic field lines approach the
39 outer penumbra, the inclination angle becomes larger, therefore
40 the cut-off frequency is lowered to a smaller value (Bel & Leroy
41 1977), and allows the channelling of upwardly propagating
42 waves of lower frequency (longer period).

3.2. Determine the MAG cut-off frequency

43 In this section, we show the steps to determine the MAG cut-
44 off frequency with the powermaps obtained with pixelised
45 wavelet filtering technique (Sych & Nakariakov 2008).
46

47 The narrowband power maps $P_p(r, \theta)$ are made into binary
48 maps see Fig. 3: the pixels below the median value
49 of the narrowband power map are labelled as 1, while others
50 are labelled as 0. Hence the regions that inhibits or al-
51 lows propagating wave in period p are differentiated. The
52 non-propagating region expands with increasing period (see
53 Fig. 2). The binary maps between two consecutive periods p
54 and $p + dp$ ($dp = 0.1$ min in our case) are compared to obtain
55 the contours that allows wave propagation in p but prohibit
56 waves in $p + dp$ (top right, Fig. 3). The cut-off period along
57 this contours is defined as $p + dp$. We also create a penumbra
58 mask (Top bottom, Fig. 3), only the pixels within the penum-
59 bra mask are considered. An example as how to obtain the
60 cut-off period in 4.2 min are displayed in Fig. 3.

61 In the 1D case, the power variation of polar angle is very
62 slight. Therefore, a further step was taken to average the
63 effect over polar angle. It become very straightforward, the
64 examples are illustrated in Fig. 6, Fig. 5 and Fig. 4 (panel c).

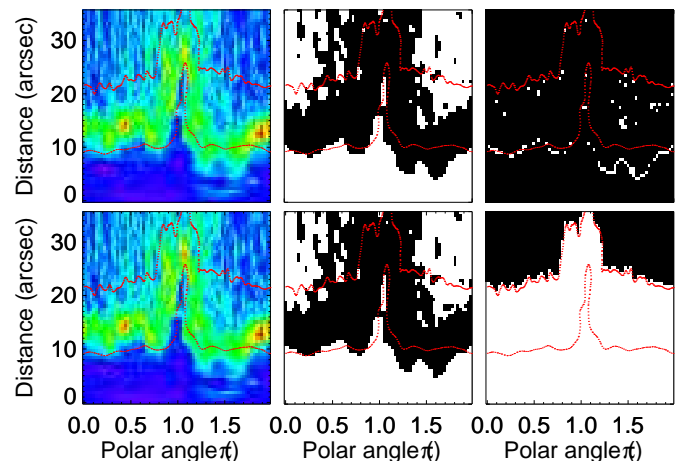


Fig. 3. Left column: the power maps in 4.1 min (top) and 4.2 min (bottom). Middle column: the binary power maps in 4.1 min (top) and 4.2 min (bottom). Right column: The difference of two consecutive binary power maps. The pixels roughly follow the umbra boundary labelled the region that allow the wave propagation in 4.2 min, but not in 4.1 min. This contour formed by these pixels is the regions defined as cut-off period at 4.1 min.

32
33
34
35
36
37
38
39
40
41
42

43

44
45
46

47
48
49
50
51
52
53
54
55
56
57
58
59
60

61
62
63
64

65

Table 1. Notations used in the paper.

Physical meaning	2D denotation	Physical meaning	1D denotation
2D spectral power map	$P_v(r, \theta)$	1D spectral power map	$P_v(r) = \langle P_v(r, \theta) \rangle_\theta$
2D spectral noise level	$\sigma(r, \theta) = \langle P_v(r, \theta) \rangle_v$	1D spectral noise level	$\sigma(r) = \langle P_v(r) \rangle_v$
2D spectral power variance	$\text{Var}(r, \theta) = \text{Var}(P_v(r, \theta))_v$	1D spectral power variance	$\text{Var}(r) = \text{Var}(P_v(r))_v$
2D spectral peak power	$P_{\max}(r, \theta) = \max(P_v(r, \theta))_v$	1D spectral peak power	$P_{\max}(r) = \max(P_v(r))_v$
2D peak period	$p_{\text{peak}}(r, \theta)$	1D peak period	$p_{\text{peak}}(r)$ for all θ
2D MAG cut-off period	$p_{\text{ac}}(r, \theta)$	1D MAG cut-off period	$p_{\text{ac}}(r)$ for all θ
2D MAG cut-off frequency	$\nu_{\text{ac}}(r, \theta) = 1/p_{\text{ac}}(r, \theta)$	1D MAG cut-off frequency	$\nu_{\text{ac}}(r) = 1/p_{\text{ac}}(r)$
...	...	1D power spread	$s(r) = \text{stdev}(P_v(r, \theta))_\theta _{v=\nu_{\text{ac}}}$

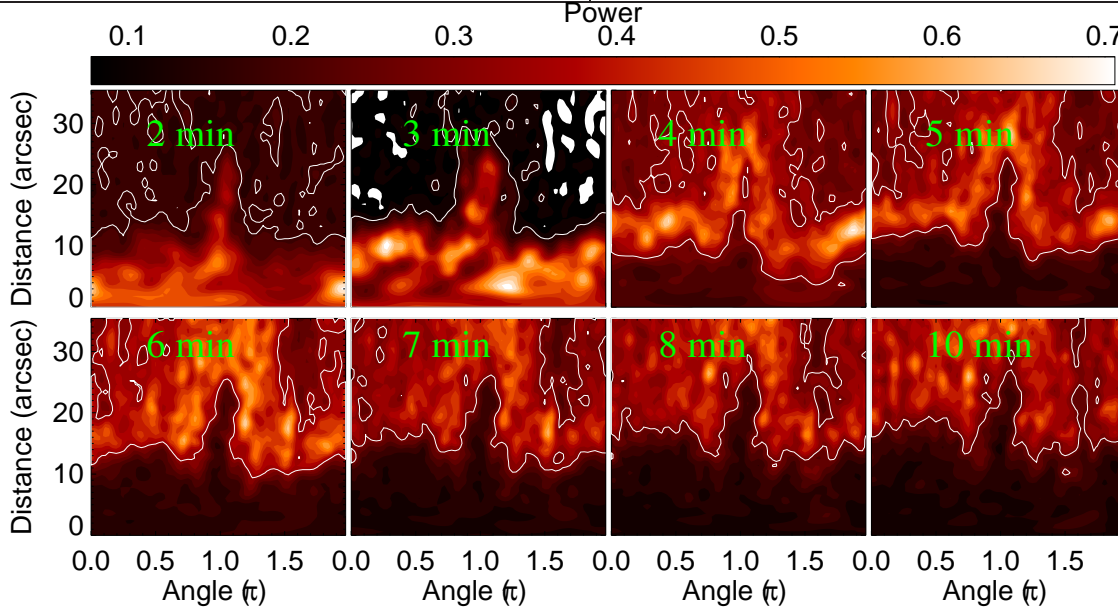


Fig. 2. Typical narrow band power maps of 304 Å bandpass in polar coordinate made for 27 Oct 2011.

4. Results

4.1. Spatial and height distribution of dominant oscillations

Based on the 1D power distribution, panel (c) of Fig. 4, Fig. 5 and Fig. 6, it is clearly seen that 3-min oscillations are very strictly constrained within the umbra region, while 5-min oscillations dominate only at a thin annulus (about 2.9 - 5.0 Mm in width) between the umbra and penumbra. Although 3-min oscillation is strongest in the umbra, it is predominant within the disks of radii about 2.1, 5.8 and 7.2 Mm in the 1700 Å (temperature minimum), 1600 Å (upper photosphere) and 304 Å (chromosphere) data, respectively. Although 3-min oscillation can propagate through both vertical and inclined magnetic field, it is constrained only in the umbra. This implies that the 3-min oscillation is not likely to originate from the solar interior. Instead, it is consistent with the acoustic resonator model (Zhugzhda 2008; Botha et al. 2011). The 5-min oscillation is well pronounced in the 1700 Å data. It appears that there is strong interaction between the magnetic fields and the ambient plasma enclosing the sunspot umbra, where the magnetic field is medium in strength and slightly inclined and has a strong longitudinal gradient. It seems there is strong p -mode absorption at the umbra border. The maximum energy transmission was predicted to occur at the height where the Alfvén speed is equivalent to the local sound speed and at an attack angle of about 30° (Cally et al. 2003; Schunker & Cally 2006). Thus the 5-min oscillation may form at the temperature minimum (about 500 km above the photosphere). The 2D power maps also confirm these results, see panels a) and b) in Fig. 4, Fig. 5, Fig. 6, Fig. 7, Fig. 8

and Fig. 9. In panel (a) of Fig. 4 and Fig. 7, the power of 3-min oscillations show variations within the umbra. This implies fine structuring inside the umbra. Stronger sources of oscillations were found better correlated with the 3-min propagating disturbances in the corona loops in 171 Å bandpass (Jess et al. 2012; Sych et al. 2012).

4.2. Correlation of the peak and cut-off frequencies

The detected cut-off frequencies are plotted versus the corresponding peak frequencies, see Fig. 10. The correlation between them is very high: the Pearson's correlation coefficients R are 0.98, 0.94 and 0.99 for the 1700 Å, 1600 Å and 304 Å data, respectively. We fitted a linear relationship ($\nu_{\text{ac}} = a\nu_{\text{peak}} + b$) to the data using the MPFITEXY routine³ (Williams et al. 2010). The MPFITEXY routine depends on the MPFIT package⁴ (Markwardt 2009). All the three lines are very close to one another, the slopes are 0.80 ± 0.01 ⁵, 0.75 ± 0.01 and 0.74 ± 0.01 for the 1700 Å, 1600 Å and 304 Å data, respectively. The results agree with the empirical relation ($\nu_{\text{peak}} \simeq 1.25\nu_{\text{ac}}$) between the peak and cut-off frequency as suggested in Bogdan & Judge (2006); Tziotziou et al. (2006), but we obtained non-zero intercepts in the linear fits, $-(0.78 \pm 0.01)$ mHz, $-(0.47 \pm 0.01)$ mHz and $-(0.78 \pm 0.01)$ mHz for 1700 Å, 1600 Å and 304 Å, respectively (see Fig. 10). Large deviations from the linear model oc-

³ <http://purl.org/mike/mpfitexy>

⁴ <http://cow.physics.wisc.edu/craigm/idl/idl.html>

⁵ The fit errors less than 0.01 were considered as 0.01.

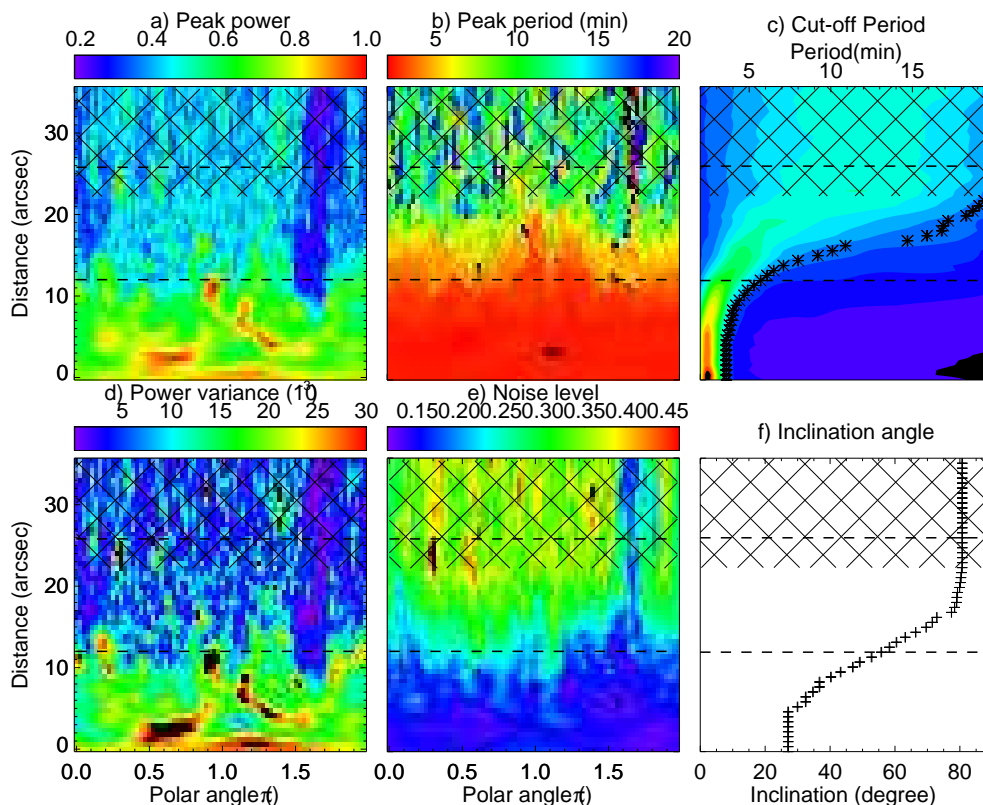


Fig. 4. The oscillating power information extracted from the 304 Å data set of the sunspot AR11131 (08 Dec 2010), shown in the polar coordinates (r and θ). The dashed lines mark the borders of the umbra and penumbra. The unreliable region is cross-hatched. a) The peak power distribution. b) The peak period distribution. c) The 1D spectral power map as a function of r and p . The contour in asterisk shows the cut-off period. d) The spectral power variance distribution. e) The spectral noise distribution. f) The reconstruction of the magnetic field inclination.

1 cur at $\nu_{\text{peak}} \simeq 3$ mHz (5-min band), strongest in 1700Å data, and
 2 also visible in 1600 Å and 304 Å as well.

3 4.3. Reconstruction of the magnetic field inclination

4 As described in Sec. A.1, the results of 1D reconstruction
 5 are illustrated in Fig. 4 (304 Å), Fig. 5 (1600 Å) and Fig. 6
 6 (1700 Å). Comparison of our results obtained with the seis-
 7 mological technique with the potential field extrapolation is
 8 shown in Fig. 11. The inclination angles were retrieved at
 9 500 km (1700 Å), 1100 km (1600 Å) and 2200 km (304 Å)
 10 above the solar surface. The magnetic inclination was esti-
 11 mated with both the theoretical acoustic cut-off frequency
 12 $\nu_0 = 5.2$ mHz and the corresponding observationally deter-
 13 mined cut-off frequency ν_0^λ , where the index λ corresponds
 14 to the observational channel used in its determination.

15 Fig. 11 shows clearly that the general profiles of field in-
 16 clinations reconstructed with the MAG cut-off at 1700 Å,
 17 1600Å and 304 Å, agree very well with the potential field
 18 extrapolation in the region from $0.2r_p$ to $0.8r_p$, where r_p
 19 is the average radius of the penumbra. The average offsets
 20 are 32.7/28.8, 27.9/26.6, 30.9/29.7 for ν_0/ν_0^λ reconstructions
 21 in 1700 Å, 1600 Å and 304 Å, respectively. The results are
 22 slightly improved by using the observed maximum cut-off
 23 frequency, but the large offsets cannot be fully removed.
 24 The reconstructed results are not sensitive to the choices
 25 of non-magnetic cut-off frequency, or the use of non-uniform
 26 ν_0 across the whole sunspot is more appropriate, but no em-
 27 pirical data are not available. This also implies that the in-
 28 clined magnetic field is not the only factor that influence the

MAG cut-off frequency, it only accounts for 60-80% of the
 29 lowering in the cut-off frequency. In the inner umbra (from
 30 0 to $0.2r_p$), the deviations from the potential field extrapo-
 31 lation are about $20^\circ - 30^\circ$. These deviations may arise from
 32 using a constant ν_0 ; choosing the observed ν_0^λ for the cor-
 33 responding bandpass appears more realistic. We obtained
 34 a flat distribution in all bandpasses in the inner umbra. It
 35 implies that the wave characteristics inside the inner umbra
 36 may be different from other regions of the sunspot, or that
 37 the impact of the plasma temperature needs to be consid-
 38 ered as well. We notice that at $0.8r_p$ - $1.2r_p$ in the 1600 Å
 39 and 1700 Å data, a region of low inclination was obtained. In
 40 our method, $\cos(\pm\phi) = |\cos(180^\circ \pm \phi)|$ can not be differen-
 41 tiated (the 180° ambiguity problem, see Metcalf et al. 2006).
 42 By considering this effect, this low-inclination region in the
 43 penumbra border can be connected with the return-flux re-
 44 gion with the magnetic vector pointing downwards, instead
 45 of upwards. The green asterisk denotes the return flux in the
 46 potential magnetic field corrected into $[0^\circ, 90^\circ]$. The results
 47 are consistent with the values estimated with the use of the
 48 MAG cut-off, both in the inclination and the distance to the
 49 sunspot centre. Such behaviour is consistent with the return-
 50 flux sunspot model (Fla et al. 1982; Osherovich 1982). The
 51 return-flux region is found to spread at about $0.8r_p$ - $1.2r_p$.
 52 If we assume a parabolic shape of the magnetic field lines, the
 53 returning flux at about $0.4r_p$ - $0.6r_p$ extends to the height of
 54 about $0.14r_p$ - $0.26r_p$ and returns to the surface about 0.4 -
 55 $0.6r_p$ apart from the source. This effect is less pronounced
 56 in the 304 Å data, in which the magnetic field shows a steady
 57 extension outwards the sunspot. The agreement between the
 58

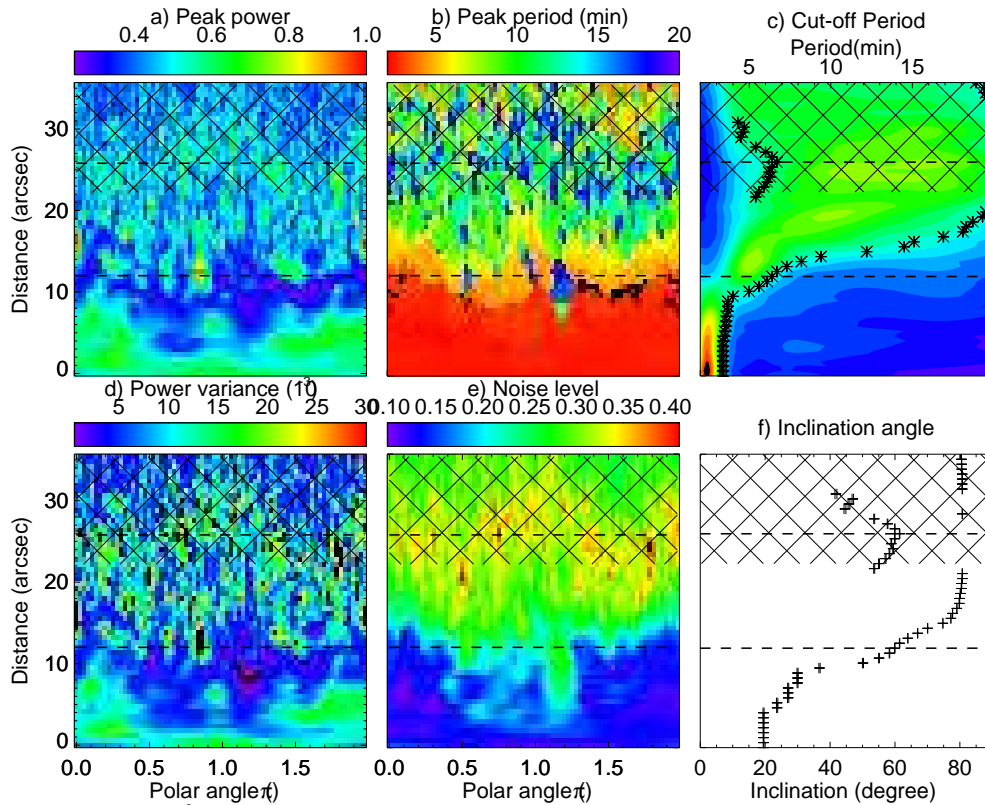


Fig. 5. The same as Fig. 4 but in 1600 Å

1 **inferred magnetic inclination and the values obtained with**
 2 **the potential field extrapolation is better in the return-flux**
 3 **region compared with the inner sunspot region. The return**
 4 **fluxes were normally found at the periphery of the sunspot**
 5 **penumbra with a weaker magnetic field and higher temper-**
 6 **ature, so we infer that other effects, e.g. radiative cooling,**
 7 **should be accounted as well to understand the lowering of**
 8 **the MAG cut-off frequency.**

9 In 2D reconstruction, we compare the reconstructed
 10 magnetic field inclination, panel (e) of Fig. 7, Fig. 8 and Fig. 9,
 11 with the potential field extrapolation shown in Fig. 12. Our
 12 method reconstructed the magnetic inclination distribution:
 13 both the global profiles, fine structure inside the sunspot um-
 14 bra and the protrusion at the penumbra. In the 1600 Å and
 15 1700 Å data, the return flux is reconstructed very well. It
 16 appears that in 2D geometry, no apparent physics modified
 17 the result, except the morphology. The potential field extrap-
 18 olation reflects the general profiles, including the protrusion
 19 structure and the return flux. The average offsets are larger,
 20 41.0, 37.8 and 37.0, which may arise from the error accumu-
 21 lation, since the outliers can not be effectively excluded.

22 5. Conclusions

23 We observed the 3D period variations of compressive oscillations
 24 in two sunspots. Our results confirm the previous findings
 25 that short-period (high-frequency) oscillations are constrained
 26 inside the sunspot umbra, while long-period (low-frequency)
 27 oscillations are mainly present outside the umbra. Longer the
 28 period is, further away the oscillations are observed from the
 29 sunspot centre. The predominant oscillation inside the umbra is
 30 the well-known 3-min oscillation. The variation over different
 31 heights indicates that the 3-min oscillation is not sourced from

the solar interior, rather it is more consistent with the acoustic
 resonator model (Zhugzhda 2008; Botha et al. 2011). The
 5-min oscillations form a ring-shape at the umbra border. We
 may speculate that the strong power of 5-min oscillations may
 indicate strong interaction of acoustic waves with the magnetic
 field, where the local condition favoured the absorption of global
 solar p -modes (Cally et al. 2003; Schunker & Cally 2006). We
 seismologically reconstructed the magnetic field inclination
 with the use of the Bel & Leroy (1977) formalism, and found
 its results to be consistent with the results obtained with poten-
 tial field extrapolation. It confirmed the conclusion in
 Bel & Leroy (1977) that the inclined magnetic field lowers
 the cut-off frequency. The MAG-reconstructed magnetic incli-
 nations are generally larger than the potential field extrap-
 olation. The small discrepancy may be attributed to the other
 effects, e.g. radiative cooling (Centeno et al. 2006, 2009;
 Felipe et al. 2010). The effect of the magnetic field inclination
 accounts for about 60-80% of the lowering in the cut-off fre-
 quency. The seismological method applied in our study pro-
 vides an alternative way to reconstruct the magnetic field.
 Moreover, it may provide the boundary or initial conditions
 for the magnetic field extrapolation.

In our method, we assumed $\beta \ll 1$, which may be incor-
 rect in some parts of the sunspots. The method can be im-
 proved by considering an observational or empirical β pro-
 files at various heights of the sunspots. If the 3D magnetic
 field vector field is available, the magnetic field strength and
 inclination can be calculated, we are able to reconstruct the
 sound speed and local temperature profiles in both 1D and
 2D at various heights.

Acknowledgements. DY is supported by MPAGS studentship. MAGPACK2
 package for computing solar magnetic fields was developed by T. Sakurai.
 The work was supported by the RFBR grant N12-02-91161-GFEN_a, 10-02-
 00153-a, Marie Curie International Research Staff Exchange Scheme Fellow-

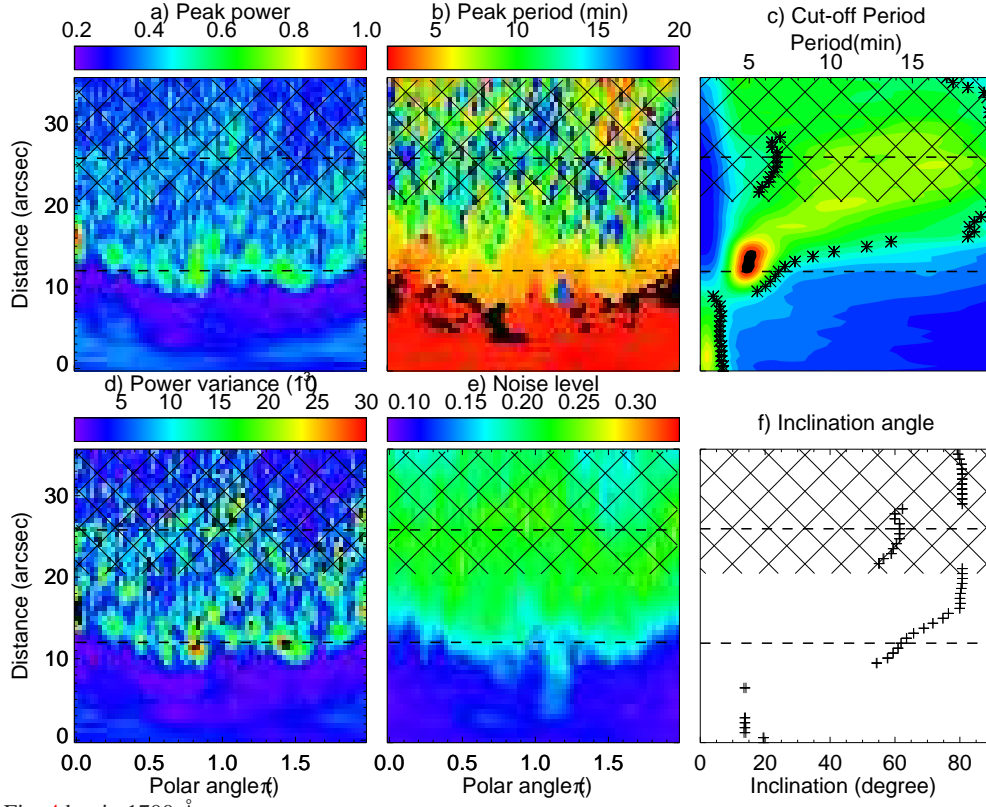


Fig. 6. The same as Fig. 4 but in 1700 Å

1 ship PIRSES-GA-2011-295272 and the Ministry of Education and Science of
 2 the Russian Federation. The AIA data were used as courtesy of the SDO AIA
 3 science team. This research has made use of NASA's Astrophysics Data System.

4 **Appendix A: The derivation of cut-off frequency in** 5 **strong field approximation**

To study the linear propagation of low-frequency waves in an isothermal atmosphere permeated by a uniform magnetic field, a co-ordinate system was chosen with z -axis along the gravitational field \mathbf{g} , the magnetic field is taken in the (x, z) plane (Bel & Mein 1971), so that

$$\mathbf{g} = (0, 0, g_z) \quad (\text{A.1})$$

$$\mathbf{B} = (B_x, 0, B_z). \quad (\text{A.2})$$

The equilibrium state are

$$\rho_{\text{eq}} = \rho_0 \exp(-z/H) \quad (\text{A.3})$$

$$P_{\text{eq}} = P_0 \exp(-z/H) \quad (\text{A.4})$$

6 where ρ_0 and P_0 are the density and pressure at a reference level,
 7 H is the scale height: $H = a^2/\gamma |g|$.

The local dispersion of magneto-acoustic gravity waves is (see Eq. (6) in Bel & Mein 1971)

$$\omega^4 - [i\gamma g k_z + (a^2 + V_A^2)k^2]\omega^2 + a^2 k^2 (\mathbf{k} \cdot \mathbf{b})^2 V_A^2 + (\gamma - 1)g^2(k^2 - k_z^2) + i\gamma g b_z k^2 (\mathbf{k} \cdot \mathbf{b}) V_A^2 = 0. \quad (\text{A.5})$$

The denotations follow (Bel & Mein 1971; Bel & Leroy 1977). This leads to the dispersion relation in Eq.(1) in Bel & Leroy (1977) (also note the typo therein.):

$$\omega^4 - [i\gamma g k_z + (a^2 + V_A^2)k_z^2]\omega^2 + a^2 k_z^4 V_A^2 \cos^2 \theta + i\gamma g k_z^3 V_A^2 \cos^2 \theta = 0. \quad (\text{A.6})$$

Here $k_{\perp} = 0$ is used in this step. Then we used the denotations: $l = V_A/a$, $m = V_A/a \cos \theta = l \cos \theta$, $k_z = \alpha + i\beta$, where α is the real wave number and β is the damping factor for positive values, or growth factor for negative values, and the normalized dimensional variables: $\omega' = H\omega/a$, $Hk_z = x + iy$. After insertion of these variables, the dispersion relation is expressed as,

$$\omega'^4 - [iHk_z + (1 + l^2)(Hk_z)^2]\omega'^2 + [(Hk_z)^4 + i(Hk_z)^3]m^2 = 0. \quad (\text{A.7})$$

For a wave $\delta \mathbf{v} = \delta \mathbf{v}_0 \exp i[k_z z - \omega t]$ with $k_z = \alpha + i\beta$, it become non-propagating wave, if α approaches zero, then $Hk_z = iy$, therefore Eq. (A.7) becomes

$$\omega'^4 + [y + (1 + l^2)y^2]\omega'^2 + (y^4 + y^3)m^2 = 0. \quad (\text{A.8})$$

This equation agrees with Eq.(16) in Bel & Mein (1971). In the strong field (low plasma beta) approximation,

$$l \rightarrow \infty \quad (\text{A.9})$$

$$m \rightarrow \infty \quad (\text{A.10})$$

$$\frac{l}{m} = \frac{1}{\cos \theta}. \quad (\text{A.11})$$

Now, Eq.(A.8) is rephased into,

$$y^2 \left[\left(y + \frac{1}{2} \right)^2 + \frac{\omega'^2}{\cos^2 \theta} - \frac{1}{4} \right] = 0. \quad (\text{A.12})$$

There is solutions for y in real space, only if

$$\frac{\omega'^2}{\cos^2 \theta} - \frac{1}{4} \leq 0.$$

Therefore the cut-off angular frequency is defined as $\omega'_c = \frac{1}{2} \cos \theta$. In dimensional variable, $\omega_c = 2\pi\nu_c = \frac{a}{2H} \cos \theta$. So

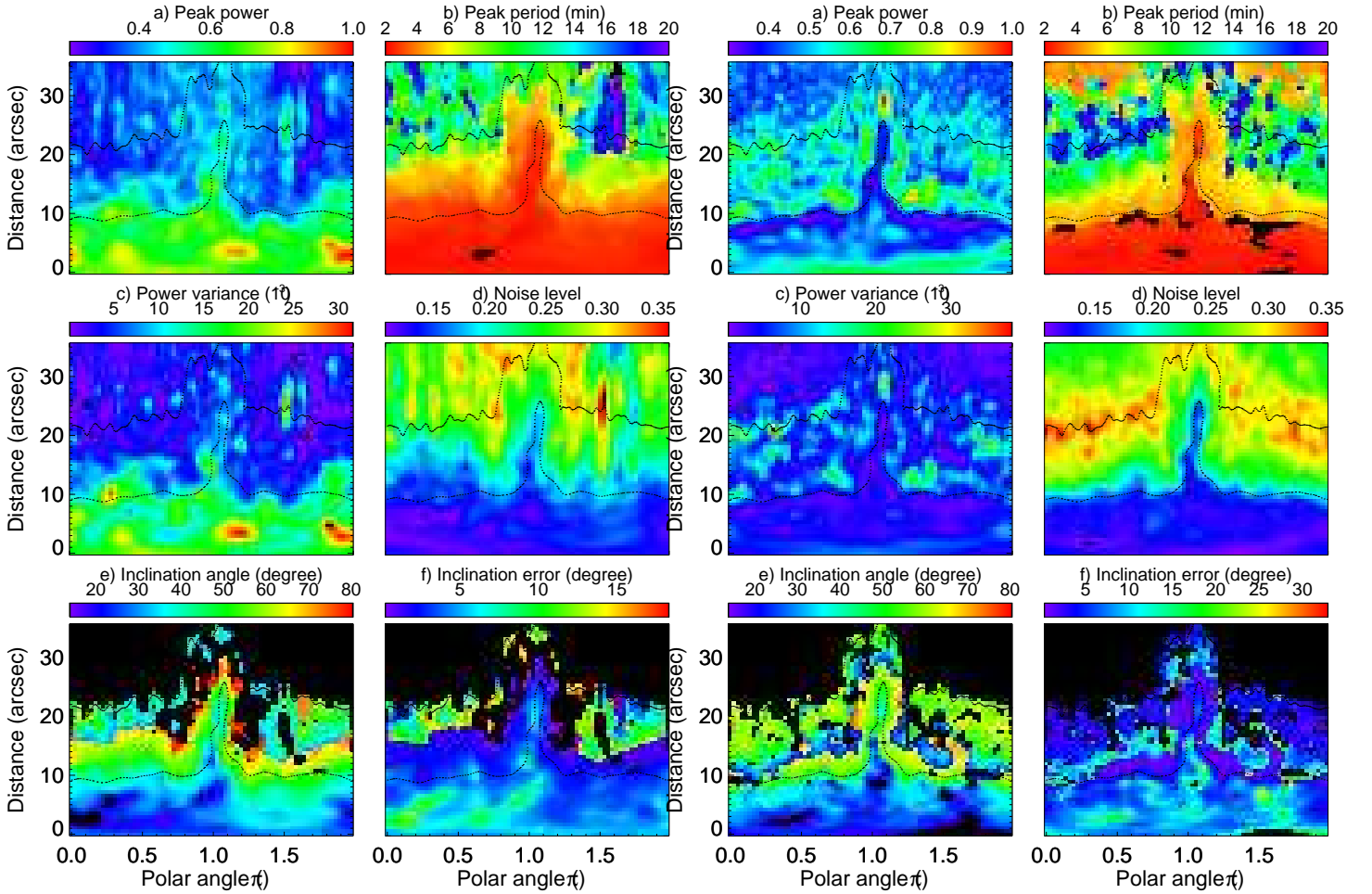


Fig. 7. a) - d) are the same as a), b), d) and e) in Fig. 4. e) and f) are the inclination angle and its uncertainty reconstructed in 2D.

Fig. 8. The same as in Fig. 7 but in 1600 Å

the cut-off frequency in strong field (low plasma beta) approximation, is given by

$$\nu_c = \nu_0 \cos \theta,$$

1 where $\nu_0 = a/4\pi H = \gamma g/4\pi a$.

2 *Appendix A.1: 1D reconstruction in symmetric sunspot (08*
3 *Dec 2010)*

4 *Appendix A.1.1: Reconstruction of field line inclination by*
5 *MAG cut-off*

6 For the symmetric sunspot observed AR11131 (08 Dec 2010),
7 we present the example of 304 Å data in Fig. 4. The distribution
8 of the peak power $P_{max}(r, \theta)$ and the corresponding peak period
9 $p_{peak}(r, \theta)$ are illustrated in Fig. 4 (a) and Fig. 4 (b), respectively.
10 The dominant oscillating power fills in the umbra and gradually
11 decreases further out in the penumbra and arcade region. In the
12 umbra, the peak period is the well-known chromospheric 3-min
13 oscillation (see review paper [Bogdan & Judge 2006](#)). It fills
14 up the whole umbra and a tiny part of the penumbra. In the
15 penumbra, the peak period gradually increases with the radial
16 distance from sunspot centre, indicating the modification of the
17 cut-off frequency by inclined magnetic field lines. The variation
18 with the polar angle is found to be very small. We averaged the
19 power along the polar angles and obtained the normalised power
20 $P_v(r)$ as a function of the distance to the sunspot centre, r , and
21 the frequency ν , as shown in Fig. 4 (c). We defined the contour

of the global median in $P_v(r)$ as the curve of the cut-off period
 $p_{ac}(r)$ (or frequency $\nu_{ac}(r) = 1/p_{ac}(r)$, see Fig. 4 (c)).

22 According to [Bel & Leroy \(1977\)](#), the MAG cut-off frequency
23 in the low- β approximation is modified when the mag-
netic field line is inclined from the vertical direction, $\nu_{ac} =$
 $\nu_0 \cos \phi$. We estimated the inclination angle ϕ by

$$\phi(r) = \arccos \frac{\nu_{ac}(r)}{\nu_0} = \arccos \frac{p_0}{p_{ac}(r)} \quad (\text{A.13})$$

where $\nu_0 = 5.2$ mHz ($p_0 = 3.2$ min) is the acoustic cut-off fre-
quency (period) (see Fig. 4 (f)).

Appendix A.1.2: Error and significance analysis

26 According to Eq. (A.13), the uncertainty of ϕ is calculated as

$$\Delta\phi(r) = \frac{\Delta\nu_{ac}(r)}{\sqrt{\nu_0^2 - \nu_{ac}^2(r)}} = \frac{\cos^2 \phi}{\sqrt{1 - \cos^2 \phi}} \frac{\Delta p_{ac}(r)}{p_0}, \quad (\text{A.14})$$

which requires the estimation of Δp_{ac} . This quantity can be as-
sumed to be proportional to the noise level $\sigma(r)$, and the spread
(standard deviation) of the spectral power over the polar angle
 $s(r)$. Δp_{ac} should also be inversely proportional to the maxi-
mum spectral power $P_{max}(r)$ and the square root of the number
of the data point in polar angles, $\sqrt{N_\theta}$. The noise level $\sigma(r)$
is found to vary between 0.16 and 0.36. When we normalise it
with its total median, it gives a factor between 0.52 and 1.13 to
the uncertainty. We did the same to the spread $s(r)$ and obtained

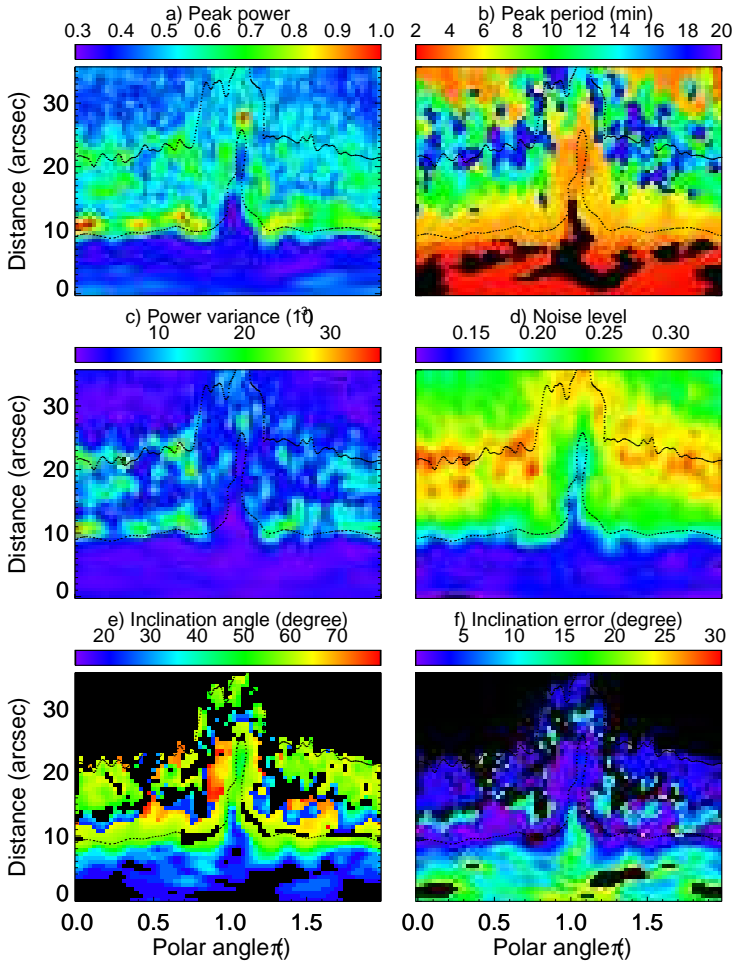


Fig. 9. The same as in Fig. 7 but in 1700 Å

another factor between 0.31 and 1.4 added to the error bar. The value of $P_{max}(r)$ changes from 1 to about 0.4 with r , giving a factor from about 1 to about 2.5 to the total error bar. We choose a constant $dp = 0.1$ min, the spectral resolution of PWF analysis, therefore the total uncertainty becomes

$$\Delta p_{ac}(r) = \frac{\sigma(r)}{\text{Med}(\sigma(r))} \frac{s(r)}{\text{Med}(s(r))} \frac{dp}{\sqrt{N_\theta} P_{max}(r)}. \quad (\text{A.15})$$

1 When the cut-off period approaches the detection limit (20
 2 min in our application), the observation of the cut-off effect be-
 3 comes less reliable. Applying this limit, we estimated the re-
 4 gions of significant measurements. We estimated the noise in
 5 the spectra as $\sigma(r, \theta) = \langle P_v(r, \theta) \rangle_v$. The noise level is illus-
 6 trated in Fig. 4 (e). It was further averaged over the polar angles,
 7 $\sigma(r) = \langle P_v(r, \theta) \rangle_{\theta, v}$. The measurements with the noise level dis-
 8 tributed above 68% (more than a standard deviation above the
 9 mean) of the noise are considered as less reliable (see the cross-
 10 hatched regions in all panels of Fig. 4). An alternative way is
 11 to consider the variance of the power maps, which reflects the
 12 contrast of the oscillating powers, giving us the significance of
 13 the measurements. We excluded 23% (lower than one standard
 14 deviation below the mean) of the smaller portion of the power
 15 variance distribution. As the results determined with the use of
 16 either power variance or noise distribution are almost similar,
 17 we utilised only the results quantified by the noise level in the
 18 significance analysis.

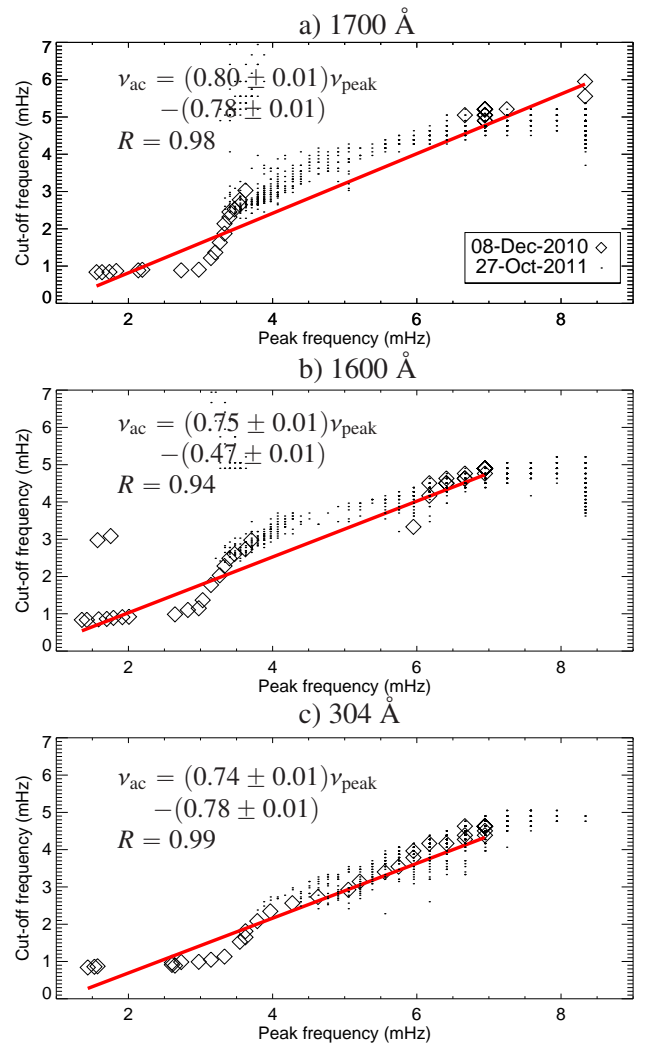


Fig. 10. Correlation between the cut-off frequency and peak frequency for 1700 Å (a), 1600 Å (b) and 304 Å (c) data. The diamond symbols represent the measurement at sunspot AR11131 observed on 08 Dec 2010, while dot symbols indicate the data of sunspot AR11330 observed on 27 Oct 2011. The data are fitted with a linear relationship $\nu_{ac} = a\nu_{peak} + b$, as plotted in red solid line. The fit parameters, as well as the Pearson's correlation coefficient, are displayed in each panel.

Appendix A.2: 2D reconstruction in asymmetric sunspot (27 Oct 2011)

19
 20
 21 In 2D spectral power maps, we consider the areas with the spec-
 22 tral power above the median of the corresponding narrow-band
 23 power map as regions that allowed upward propagating MAG
 24 waves. The borders of these areas were defined as contours of
 25 the MAG cut-off. By labelling the cut-off contours, we were able
 26 to reconstruct the field line inclination.

The reconstruction steps are similar to those in the 1D case. The estimation of the error, $\Delta p_{ac}(r, \theta)$, is simplified,

$$\Delta p_{ac}(r, \theta) = \frac{\sigma(r, \theta)}{\text{Med}(\sigma(r, \theta))} \frac{dp}{P_v(r, \theta)} \quad (\text{A.16})$$

27 We masked out the regions with the less significant measure-
 28 ments. The masks were designed with two criteria: 1) the pixel
 29 should be within the penumbra and umbra; 2) the noise level
 30 in that pixel should not exceed the 68% level in $\sigma(r, \theta)$ distri-
 31 bution. Only the measurements within the mask are shown in
 32 Fig. 7, Fig. 8 and Fig. 9

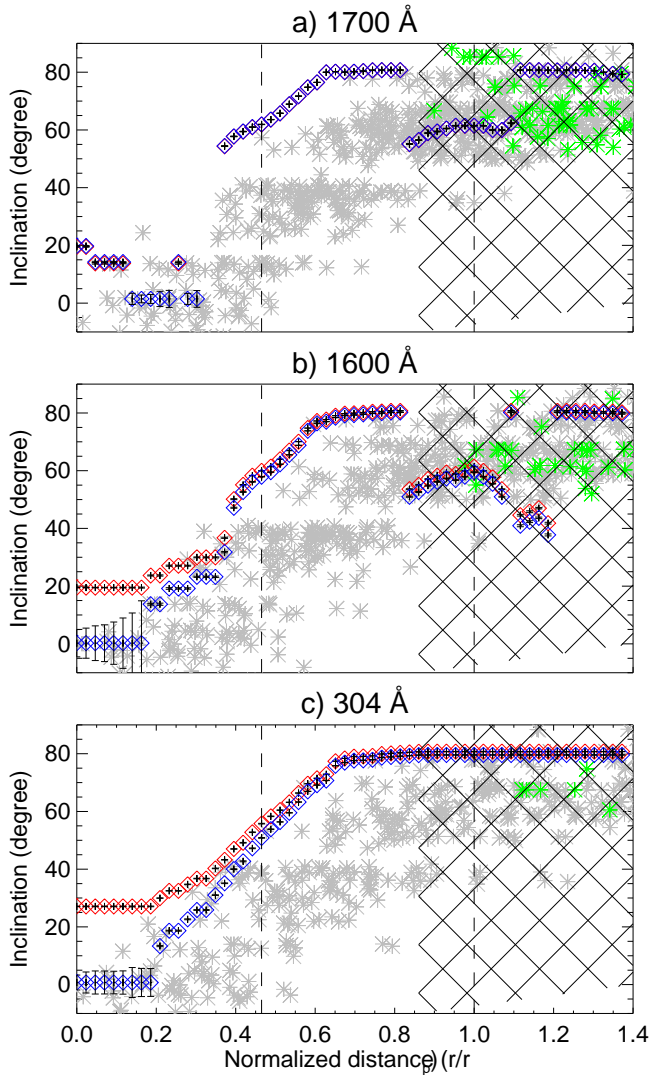


Fig. 11. Comparison of magnetic field inclination reconstructed by magneto-acoustic cut-off with potential field extrapolation for sunspot AR11131 (08 Dec 2010) in 1700 Å (a), 1600 Å (b) and 340 Å (c) bandpasses. The inclination angles obtained with the potential field extrapolation are represented in grey asterisk as the scatter plot, while the data in green asterisks denote the absolute values of inclinations of the return flux. The inclination angles reconstructed with $\nu_0 = 5.2$ mHz are plotted in the red diamonds, while those reconstructed with the observational maximum cut-off frequency ν_0^t are plotted in blue diamonds. The dashed lines show the border of the sunspot umbra and penumbra. The cross-hatched region marks the measurements below the significant level.

1 Appendix A.3: Magnetic field extrapolation

2 We compare the field reconstruction with 3D magnetic field ex-
 3 trapolation. Potential (current-free) fields were extrapolated us-
 4 ing the MAGPACK2 package (Sakurai 1982). The current-free
 5 model in this code is based on the Green's function method and
 6 requires a line-of-sight magnetogram as the bottom boundary
 7 condition. Although, we can not *a priori* exclude the presence
 8 of the electric currents in the considered volume, we have cho-
 9 sen this model because of the following reasons: 1) both of ARs
 10 did not produce any flares within or close to our observational
 11 intervals; 2) we are interested in field structures in the layers be-
 12 low the corona where the dense material can influence the field
 13 inclination. Therefore, the choice of the non-potential field is
 14 unlikely to produce better approximation at these heights.

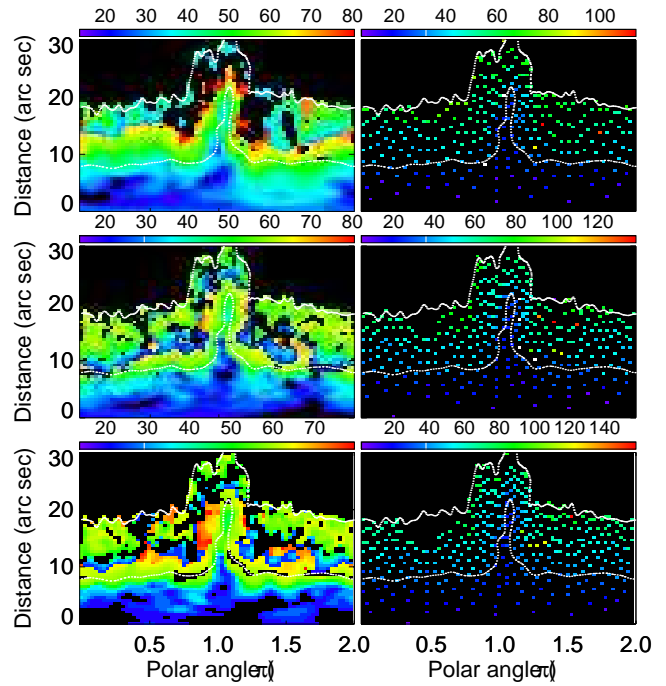


Fig. 12. Left column: magnetic field inclination obtained with ν_0 reconstruction. Right column: the inclination angle obtained from potential field extrapolation for AR11330 on 27 Oct 2011. From top to bottom rows, the panels correspond to 304 Å, 1600 Å and 1700 Å data. The dotted lines mark the umbra and penumbra borders.

Fig. A.1 presents a 2D projection of reconstructed mag- 15
 netic field lines overlaid on the photospheric line-of-sight mag- 16
 netogram (a) sunspot AR11131 (08 Dec 2010) and (b) sunspot 17
 AR11330 (27 Oct 2011). The colour coding represents the mag- 18
 netic field strength, using blue for southern (negative) and red 19
 for northern (positive) polarities. For the sunspot AR11131, we 20
 selected sub-area of $160'' \times 160''$ from the SOHO/MDI full-disk 21
 magnetogram taken at 04:51 UT, as shown in Fig. A.1(a). For 22
 the sunspot AR11330, the HMI line-of-sight magnetogram was 23
 obtained as a level-1.5 FITS file. A larger size of $300'' \times 300''$ 24
 was selected to include the sufficient amount of positive polarity 25
 following the main sunspot. The magnetic field was computed 26
 with a $2''$ mesh spacing using a spherical boundary. 27

References

Bel, N. & Leroy, B. 1977, A&A, 55, 239 29
 Bel, N. & Mein, P. 1971, A&A, 11, 234 30
 Bloomfield, D. S., Lagg, A., & Solanki, S. K. 2007, ApJ, 671, 1005 31
 Boerner, P., Edwards, C., Lemen, J., et al. 2011, Sol. Phys., 316 32
 Bogdan, T. J. & Judge, P. G. 2006, Royal Society of London Philosophical Trans- 33
 actions Series A, 364, 313 34
 Botha, G. J. J., Arber, T. D., Nakariakov, V. M., & Zhugzhda, Y. D. 2011, ApJ, 35
 728, 84 36
 Cally, P. S., Crouch, A. D., & Braun, D. C. 2003, MNRAS, 346, 381 37
 Centeno, R., Collados, M., & Trujillo Bueno, J. 2006, ApJ, 640, 1153 38
 Centeno, R., Collados, M., & Trujillo Bueno, J. 2009, ApJ, 692, 1211 39
 De Moortel, I., Ireland, J., Hood, A. W., & Walsh, R. W. 2002, A&A, 387, L13 40
 De Pontieu, B., Erdélyi, R., & De Moortel, I. 2005, ApJ, 624, L61 41
 De Pontieu, B., Erdélyi, R., & James, S. P. 2004, Nature, 430, 536 42
 de Wijn, A. G., McIntosh, S. W., & De Pontieu, B. 2009, ApJ, 702, L168 43
 Felipe, T., Khomenko, E., Collados, M., & Beck, C. 2010, ApJ, 722, 131 44
 Fla, T., Skumanich, A., & Osherovich, V. A. 1982, ApJ, 261, 700 45
 Fontenla, J. M., Avrett, E. H., & Loeser, R. 1993, ApJ, 406, 319 46
 Jefferies, S. M., McIntosh, S. W., Armstrong, J. D., et al. 2006, ApJ, 648, L151 47
 Jess, D. B., De Moortel, I., Mathioudakis, M., et al. 2012, ApJ, 757, 160 48
 Lemen, J. R., Title, A. M., Akin, D. J., et al. 2011, Sol. Phys., 172 49

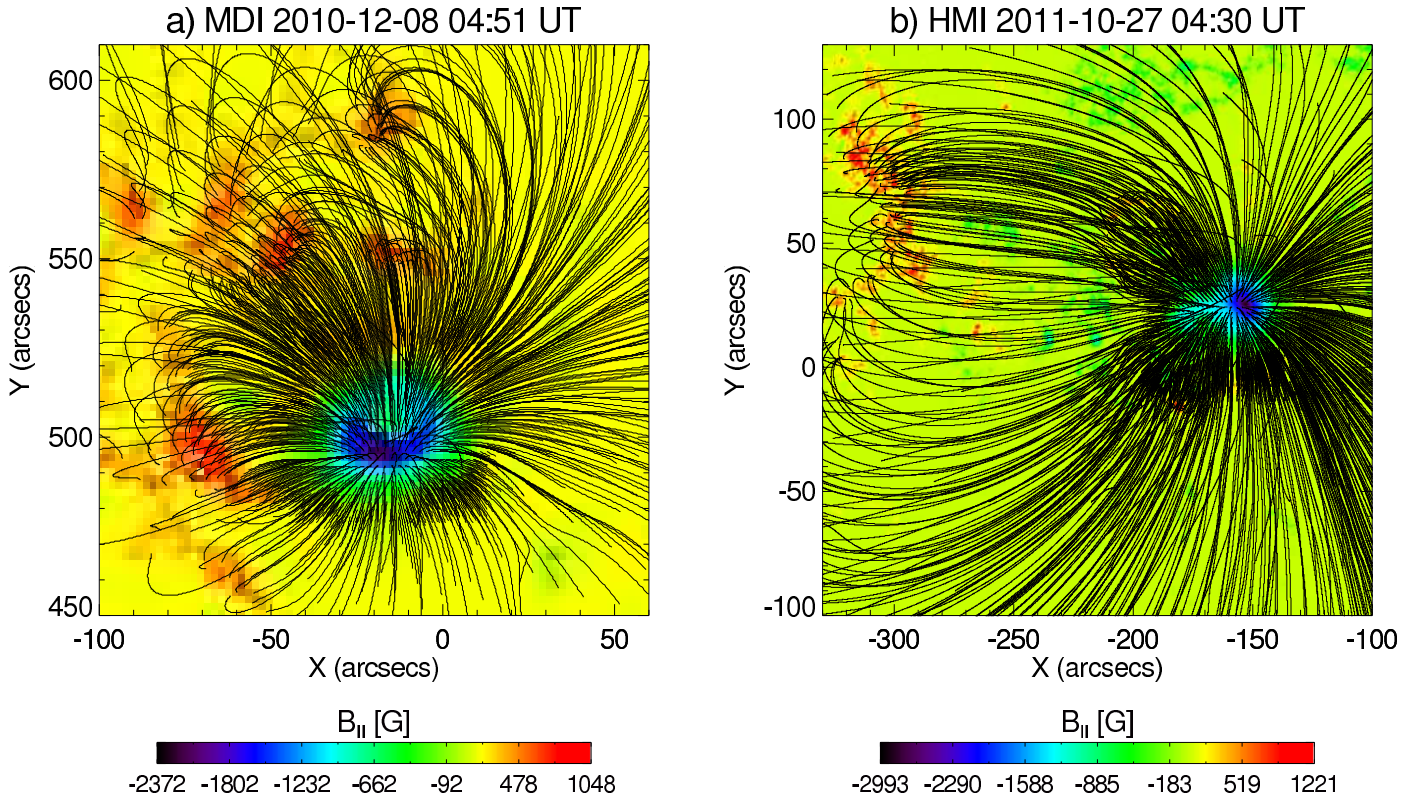


Fig. A.1. Results of the potential field extrapolation using the MDI magnetogram for sunspot AR11131 on 08 Dec 2010 (a) and with the HMI magnetogram for sunspot AR11330 on 27 Oct 2011 (b).

- 1 Loughhead, R. E. & Bray, R. J. 1958, *Australian Journal of Physics*, 11, 177
- 2 Markwardt, C. B. 2009, in *Astronomical Society of the Pacific Conference Series*, Vol. 411, *Astronomical Data Analysis Software and Systems XVIII*, ed. D. A. Bohlender, D. Durand, & P. Dowler, 251
- 3 Marsh, M. S., Walsh, R. W., & Plunkett, S. 2009, *ApJ*, 697, 1674
- 4 McIntosh, S. W. & Jefferies, S. M. 2006, *ApJ*, 647, L77
- 5 Metcalf, T. R., Leka, K. D., Barnes, G., et al. 2006, *Sol. Phys.*, 237, 267
- 6 Osherovich, V. A. 1982, *Sol. Phys.*, 77, 63
- 7 Reznikova, V. E. & Shibasaki, K. 2012, *ApJ*, 756, 35
- 8 Reznikova, V. E., Shibasaki, K., Sych, R. A., & Nakariakov, V. M. 2012, *ApJ*, 746, 119
- 9 Sakurai, T. 1982, *Sol. Phys.*, 76, 301
- 10 Schunker, H. & Cally, P. S. 2006, *MNRAS*, 372, 551
- 11 Suematsu, Y., Shibata, K., Neshikawa, T., & Kitai, R. 1982, *Sol. Phys.*, 75, 99
- 12 Sych, R., Zaqarashvili, T. V., Nakariakov, V. M., et al. 2012, *A&A*, 539, A23
- 13 Sych, R. A. & Nakariakov, V. M. 2008, *Sol. Phys.*, 248, 395
- 14 Tziotziou, K., Tsiropoula, G., Mein, N., & Mein, P. 2006, *A&A*, 456, 689
- 15 Wang, T. J., Ofman, L., Davila, J. M., & Mariska, J. T. 2009, *A&A*, 503, L25
- 16 Williams, M. J., Bureau, M., & Cappellari, M. 2010, *MNRAS*, 409, 1330
- 17 Yuan, D. & Nakariakov, V. M. 2012, *A&A*, 543, A9
- 18 Yuan, D., Nakariakov, V. M., Chorley, N., & Foullon, C. 2011, *A&A*, 533, A116
- 19 Zhugzhda, I. D. & Dzhililov, N. S. 1984, *A&A*, 132, 45
- 20 Zhugzhda, Y. D. 2008, *Sol. Phys.*, 251, 501